2017

Target and Beam-Target Spin Asymmetries in Exclusive Pion Electroproduction for $Q^2 > 1$ GeV^2 . II. ep→ eπ°p

CLAS Collaboration

K. P. Adhikari
Old Dominion University

D. Adikaram
Old Dominion University

M. J. Amaryan
Old Dominion University, mamaryan@odu.edu

S. Bültmann
Old Dominion University, sbueltma@odu.edu

See next page for additional authors

Original Publication Citation

CLAS Collaboration, Bosted, P. E., Kim, A., Adhikari, K. P., Adikaram, D., Akbar, Z., . . . Zonta, I. (2017). Target and beam-target spin asymmetries in exclusive pion electroproduction for $Q^2 > 1$ GeV^2. II. Ep→ eπ°p. *Physical Review C, 95*(3), 035207. doi:10.1103/PhysRevC.95.035207

Target and beam-target spin asymmetries in exclusive pion electroproduction for $Q^2 > 1$ GeV^2. II. $ep \to e\pi^0 p$

P. E. Bosted,[44,*] A. Kim,[8] K. P. Adhikari,[25,29] D. Adikaram,[29,36] Z. Akbar,[12] M. J. Amaryan,[29] S. Anefalos Pereira,[16] H. Avakian,[36] R. A. Badui,[11] J. Ball,[6] I. Balossino,[15] M. Battaglieri,[17] I. Bedlinskiy,[21] A. S. Biselli,[9] S. Boiarinov,[36] W. J. Briscoe,[13] W. K. Brooks,[37] S. Bültmann,[29] V. D. Burkert,[36] T. Cao,[34,46] D. S. Carman,[36] A. Celentano,[17] S. Chandavar,[28] G. Charles,[20] T. Chetry,[28] G. Ciullo,[10,15] L. Clark,[39] L. Colaneri,[18,32] P. L. Cole,[14] M. Contalbrigo,[15] O. Cortes,[14] V. Crede,[12] A. D'Angelo,[18,32] N. Dashyan,[45] R. De Vita,[17] E. De Sanctis,[16] A. Deur,[36] C. Djalali,[34] R. Dupre,[1,20] H. Egiyan,[26,36] A. El Alaoui,[1,24,37] L. El Fassi,[1,25] L. Elouadrhiri,[36] P. Eugenio,[12] E. Fanchini,[17] G. Fedotov,[33,34] S. Fegan,[17,39] R. Fersch,[7,44] A. Filippi,[19] J. A. Fleming,[38] T. A. Forest,[14] A. Fradi,[20] Y. Ghandilyan,[45] G. P. Gilfoyle,[31] F. X. Girod,[36] D. I. Glazier,[39] W. Gohn,[8,40] E. Golovatch,[33] R. W. Gothe,[34] K. A. Griffioen,[44] M. Guidal,[24] N. Guler,[29,47] H. Hakobyan,[37,45] L. Guo,[11,36] K. Hafidi,[1] H. Hakobyan,[37,45] C. Hanretty,[12,36] N. Harrison,[36] M. Hattawy,[1] D. Heddle,[7,36] K. Hicks,[28] G. Hollis,[34] M. Holtrop,[26] S. M. Hughes,[38] D. G. Ireland,[39] E. L. Isupov,[33] D. Jenkins,[42] H. Jiang,[34] H. S. Jo,[20] K. Joo,[8] D. Keller,[28,43] G. Khachatryan,[45] M. Khandaker,[14,27] W. Kim,[23] A. Klei,[29] F. J. Klein,[5] S. Koirala,[29] V. Kubarovsky,[36] S. E. Kuhn,[29] L. Lanza,[18] P. Lenisa,[15] K. Livingston,[39] H. Y. Lu,[34] I. J. D. MacGregor,[39] N. Markov,[8] M. Mayer,[29] M. E. McCracken,[4] B. McKinnon,[39] T. Mineeva,[8,37] M. Mirazita,[16] V. I. Mokeev,[36] R. A. Montgomery,[39] A. Movsisyan,[15] C. Munoz Camacho,[20] G. Murdoch,[39] P. Nadel-Turonski,[5,36] A. Ni,[23] S. Niccolai,[20] G. Niculescu,[22] M. Osipenko,[17] A. I. Ostrovidov,[12] M. Paolone,[35] R. Paremuzyan,[26] K. Park,[34,36] E. Pasyuk,[36] W. Phelps,[11] S. Pisano,[16,20] O. Pogorelko,[21] J. W. Price,[3] Y. Prok,[41] D. Protopopescu,[39] A. J. R. Puckett,[8] B. A. Raue,[11,36] M. Ripani,[17] A. Rizzo,[18,32] G. Rosner,[39] P. Rossi,[16,36] P. Roy,[12] F. Sabatié,[6] M. S. Saini,[12] R. A. Schumacher,[4] E. Seder,[8] Y. G. Sharabian,[36] Iu. Skorodumina,[33,34] G. D. Smith,[38] D. Sokhan,[39] N. Sparveris,[35] I. Stankovic,[38] S. Stepanyan,[36] P. Stoler,[30] I. I. Strakovsky,[13] S. Strauch,[34] M. Taiuti,[17] Ye Tian,[34] B. Torayev,[29] M. Ungaro,[8,36] H. Voskanyan,[45] E. Voutier,[20] N. K. Walford,[5] D. P. Watts,[38] X. Wei,[36] L. B. Weinstein,[29] N. Zachariou,[38] J. Zhang,[29,36] Z. W. Zhao,[29,34] and I. Zonta[18,32]

(CLAS Collaboration)

[1]*Argonne National Laboratory, Argonne, Illinois 60439, USA*
[2]*Arizona State University, Tempe, Arizona 85287-1504, USA*
[3]*California State University, Dominguez Hills, Carson, California 90747, USA*
[4]*Carnegie Mellon University, Pittsburgh, Pennsylvania 15213, USA*
[5]*Catholic University of America, Washington, DC 20064, USA*
[6]*Irfu/SPhN, CEA, Université Paris-Saclay, 91191 Gif-sur-Yvette, France*
[7]*Christopher Newport University, Newport News, Virginia 23606, USA*
[8]*University of Connecticut, Storrs, Connecticut 06269, USA*
[9]*Fairfield University, Fairfield, Connecticut 06824, USA*
[10]*Universita' di Ferrara, 44121 Ferrara, Italy*
[11]*Florida International University, Miami, Florida 33199, USA*
[12]*Florida State University, Tallahassee, Florida 32306, USA*
[13]*George Washington University, Washington, DC 20052, USA*
[14]*Idaho State University, Pocatello, Idaho 83209, USA*
[15]*INFN, Sezione di Ferrara, 44100 Ferrara, Italy*
[16]*INFN, Laboratori Nazionali di Frascati, 00044 Frascati, Italy*
[17]*INFN, Sezione di Genova, 16146 Genova, Italy*
[18]*INFN, Sezione di Roma Tor Vergata, 00133 Rome, Italy*
[19]*INFN, Sezione di Torino, 10125 Torino, Italy*
[20]*Institut de Physique Nucléaire, CNRS/IN2P3 and Université Paris Sud, Orsay, France*
[21]*Institute of Theoretical and Experimental Physics, Moscow, 117259, Russia*
[22]*James Madison University, Harrisonburg, Virginia 22807, USA*
[23]*Kyungpook National University, Daegu 41566, Republic of Korea*
[24]*LPSC, Université Grenoble-Alpes, CNRS/IN2P3, Grenoble, France*
[25]*Mississippi State University, Mississippi State, Mississippi 39762-5167, USA*
[26]*University of New Hampshire, Durham, New Hampshire 03824-3568, USA*
[27]*Norfolk State University, Norfolk, Virginia 23504, USA*
[28]*Ohio University, Athens, Ohio 45701, USA*
[29]*Old Dominion University, Norfolk, Virginia 23529, USA*
[30]*Rensselaer Polytechnic Institute, Troy, New York 12180-3590, USA*
[31]*University of Richmond, Richmond, Virginia 23173, USA*
[32]*Universita' di Roma Tor Vergata, 00133 Rome, Italy*
[33]*Skobeltsyn Institute of Nuclear Physics, Lomonosov Moscow State University, 119234 Moscow, Russia*
[34]*University of South Carolina, Columbia, South Carolina 29208, USA*

[35]*Temple University, Philadelphia, Pennsylvania 19122, USA*
[36]*Thomas Jefferson National Accelerator Facility, Newport News, Virginia 23606, USA*
[37]*Universidad Técnica Federico Santa María, Casilla 110-V Valparaíso, Chile*
[38]*Edinburgh University, Edinburgh EH9 3JZ, United Kingdom*
[39]*University of Glasgow, Glasgow G12 8QQ, United Kingdom*
[40]*University of Kentucky, Lexington, Kentucky 40506, USA*
[41]*Virginia Commonwealth University, Richmond, Virginia 23284, USA*
[42]*Virginia Tech, Blacksburg, Virginia 24061-0435, USA*
[43]*University of Virginia, Charlottesville, Virginia 22901, USA*
[44]*College of William and Mary, Williamsburg, Virginia 23187-8795, USA*
[45]*Yerevan Physics Institute, 375036 Yerevan, Armenia*
[46]*Hampton University, Hampton, Virginia 23668, USA*
[47]*Los Alamos National Laboratory, Los Alamos, New Mexico 87544, USA*
(Received 17 November 2016; published 20 March 2017)

Beam-target double-spin asymmetries and target single-spin asymmetries were measured for the exclusive π^0 electroproduction reaction $\gamma^* p \to p\pi^0$, expanding an analysis of the $\gamma^* p \to n\pi^+$ reaction from the same experiment. The results were obtained from scattering of 6-GeV longitudinally polarized electrons off longitudinally polarized protons using the CEBAF Large Acceptance Spectrometer at Jefferson Laboratory. The kinematic ranges covered are $1.1 < W < 3$ GeV and $1 < Q^2 < 6$ GeV^2. Results were obtained for about 5700 bins in W, Q^2, $\cos(\theta^*)$, and ϕ^*. The beam-target asymmetries were found to generally be greater than zero, with relatively modest ϕ^* dependence. The target asymmetries exhibit very strong ϕ^* dependence, with a change in sign occurring between results at low W and high W, in contrast to π^+ electroproduction. Reasonable agreement is found with phenomenological fits to previous data for $W < 1.6$ GeV, but significant differences are seen at higher W. When combined with cross-sectional measurements, as well as π^+ observables, the present results will provide powerful constraints on nucleon resonance amplitudes at moderate and large values of Q^2, for resonances with masses as high as 2.4 GeV.

DOI: 10.1103/PhysRevC.95.035207

I. INTRODUCTION

This article is a companion to a previous publication [1], which presents data for the target and beam-target spin asymmetries in exclusive π^+ electroproduction for $Q^2 > 1$ GeV^2. The present article expands upon Ref. [1] to provide results for π^0 electroproduction. Briefly, the physics motivation is to study nucleon structure and reaction mechanisms via large-Q^2 pion electroproduction. The results are from the eg1-dvcs experiment, which used scattering of 6-GeV longitudinally polarized electrons off longitudinally polarized protons. Scattered electrons and electroproduced neutral pions were detected in the CEBAF Large Acceptance Spectrometer [2] (CLAS) at Jefferson Laboratory (JLab). The standard detector set of wire chambers, gas-filled Cherenkov detectors, time-of-flight scintillation counters, and electromagnetic calorimeter was augmented for this experiment with an inner calorimeter (IC). This calorimeter consists of an array of small lead-tungstate crystals, each 15 cm long and roughly 2 cm square. The IC greatly increased the acceptance for neutral pions compared to the standard setup. The primary target for this analysis consisted of a 1.5-cm-long cell with about 1 g/cm^2 of ammonia immersed in a liquid-helium bath. An auxiliary target with carbon instead of ammonia was used for background studies. The data taking relevant to the present analysis was divided into two parts, for which the target position, electron beam energy, and beam and target polarizations are listed in Table I.

For further elucidation of the physics motivation, details on the formalism, experimental overview, and details on the detection of scattered electrons, please see the companion article [1] as well as other publications from the eg1-dvcs experiment on inclusive electron scattering [3] and deep virtual Compton scattering [4].

Large four-momentum transferred Q^2 measurements of spin-averaged cross sections for exclusive π^0 electroproduction from a proton are sparse compared to π^+ production, and published results are limited to the $\Delta(1232)$ resonance region [5,6], with results at higher invariant mass W from CLAS still under analysis [7], although the beam single-spin asymmetries (A_{LU}) were published [8] several years ago. Beam-target asymmetries (A_{LL}) and target single-spin asymmetries (A_{UL}) for $ep \to e\pi^0 p$ were reported from the eg1b experiment at JLab [9] at relatively low Q^2 for an electron beam energy of 1.7 GeV. Results for A_{LL} and A_{UL} at much larger values of Q^2 from the present experiment were reported in Ref. [10], for values of the final-state invariant mass W above 2 GeV. The present analysis expands upon Ref. [10] to include $W <$ 2 GeV and provide higher statistical precision for $W > 2$ GeV through the inclusion of additional final state topologies.

II. ANALYSIS

The data analysis for π^0 electroproduction proceeded in parallel with that for π^+ electroproduction as described in the companion article, Ref. [1].

*bosted@jlab.org

TABLE I. Run period names, target position along the beam line relative to CLAS center (z), nominal beam energy (E), $P_B P_T$, and P_B, where P_B (P_T) is the beam (target) polarization, for the two running periods of the experiment.

Run period	z	E	$P_B P_T$	P_B
Part A	−58 cm	5.887 GeV	0.637 ± 0.011	0.85 ± 0.04
Part B	−68 cm	5.954 GeV	0.645 ± 0.007	0.85 ± 0.04

A. Particle identification

We analyzed π^0 electroproduction using three topologies: $ep \to e\gamma\gamma p, ep \to e\gamma(\gamma)p$, and $ep \to e\gamma\gamma(p)$. No event was counted in more than one topology. All three topologies require detection of the scattered electron and at least one photon. The $ep \to e\gamma\gamma p$ and $ep \to e\gamma\gamma(p)$ topologies require the detection of two photons with invariant mass corresponding to a π^0. The $ep \to e\gamma\gamma p$ and $ep \to e\gamma(\gamma)p$ topologies also require the detection of a proton. The cuts used to identify scattered electrons are given in Ref. [1].

1. Proton identification

Protons were identified by requiring a positively charged track with a time of arrival at the scintillation counters within 0.7 ns (approximately 3σ) of that predicted from the time of arrival of the electron in the event. This timing cut removed all charged pions from the sample but allowed between 10% to 100% of K^+, depending on kaon momentum. These events were removed by the missing mass cut discussed below. Positrons were removed from the sample by requiring small (or no) signal in the Cherenkov detector and small deposited energy in the electromagnetic calorimeter (EC). Also required were a vertex position reconstructed (with a resolution of 5 to 8 mm) within 4 cm of the nominal target center and a polar scattering angle between 15 and 48 deg.

2. Photon identification

Photons in the EC were identified with the following criteria: no associated track (to ensure neutrality); energy greater than 0.3 GeV (to have sufficiently good energy resolution); time of arrival at the EC in agreement with the scattered electron time within 3 ns (to reduce the rate of accidental coincidences); and an antibremsstrahlung cut of 3.4 deg. A photon was considered to be a candidate for bremsstrahlung from the scattered electron if the opening angle between the electron and the photon was less than 3.4 deg at either the target vertex or the first drift chamber. The reason that both places were checked is that the electron undergoes a significant azimuthal rotation in the target solenoid.

Photons in the IC were identified by requiring a deposited energy of at least 0.2 GeV (to ensure adequate energy resolution) and a time of arrival within 2 ns of that calculated from the scattered electron arrival time (to reject random background). Single photons in the IC [for the topology $ep \to e\gamma(\gamma)p$] were not considered, because study of the electron-proton missing mass distributions revealed a large background of events in which the IC particle was an electron

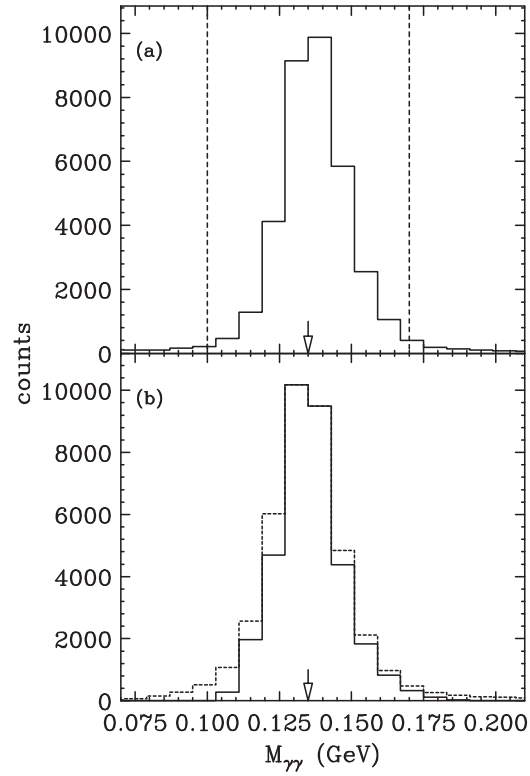

FIG. 1. Two-photon invariant mass distributions for (a) $ep \to e\gamma\gamma p$ and (b) $ep \to e\gamma\gamma(p)$, with all relevant exclusivity cuts applied. The vertical dashed lines show the cuts used for $ep \to e\gamma\gamma p$. The solid (dashed) curve in the lower panel is with (without) the application of the χ^2 cut discussed in the text.

(rather than a photon), and the missing particle was a positron, i.e.,

$$e^- p \to e^- \ (\text{in IC}) \ \ p \ (\text{in CLAS}) \times e^- \ (\text{in CLAS}) \ \ (e^+, \ \text{missing}).$$

In this case, the electron in CLAS and the missing positron are the products of the decays of π^0, η, or other mesons. A scintillator hodoscope array placed in front of the IC would have allowed for rejection of charged particles but unfortunately was not reliably operational for this experiment.

3. π^0 identification

For topologies $ep \to e\gamma\gamma p$ and $ep \to e\gamma\gamma(p)$, a π^0 was identified using the invariant mass of the photon pair. Figure 1(a) shows the mass distributions for events passing all other exclusivity cuts for the topology $ep \to e\gamma\gamma p$. The background under the peak is very small (less than 1.5%) for this topology. The vertical dashed lines show the cuts used: $0.10 < M_{\gamma\gamma} < 0.17$ GeV.

The two-photon mass distribution for topology $ep \to e\gamma\gamma(p)$ is shown in Fig. 1(b). The dashed curve is for events passing the electron-meson missing mass cut discussed below. There is more background under the π^0 peak than for topology $ep \to e\gamma\gamma p$ (as evidenced by the enhancement around 0.1 GeV). Rather than using a simple two-photon mass

cut, it was found that a more complicated cut was better at removing background events. The solid curve is with the cut $\chi^2 < 4$, where χ^2 is defined in the next paragraph. The cut value was chosen empirically to minimize the uncertainty in the final asymmetry results.

In order to get the best possible determination of electron-pion missing mass, we adjusted the energy of each of the two photons such that the invariant mass was exactly equal to the π^0 mass M_0. We did not adjust the photon angles, because the energy resolution is the dominant contribution. We can define

$$M_0^2/M_{\gamma\gamma}^2 = (1 + c_1\sigma_1)(1 + c_2\sigma_2), \quad (1)$$

where $M_{\gamma\gamma}$ is the measured invariant two-photon mass, c_1 and c_2 are coefficients to be determined by minimizing $\chi^2 = c_1^2 + c_2^2$, and the relative photon energy resolutions σ_i were approximated by

$$\sigma_i = 0.01 + \frac{0.05}{\sqrt{E_\gamma}} \quad \text{for} \quad \text{IC},$$

$$\sigma_i = 0.02 + \frac{0.12}{\sqrt{E_\gamma}} \quad \text{for} \quad \text{EC}.$$

After the fit was done, the photon energies were scaled by $(1 + c_i\sigma_i)$.

B. Exclusivity kinematic cuts

For all three topologies, kinematic cuts were placed to improve the signal-to-noise ratio. The value of kinematic cuts is twofold. First, most of the kinematic quantities have a wider distribution for bound nucleons (in target materials with atomic number $A > 2$) than for free protons. Kinematic cuts therefore reduce the dilution of the signal of interest (scattering from polarized free protons) compared to the background from unpolarized nucleons in materials with $A > 2$. Second, kinematic cuts are needed to isolate single-meson production from multimeson production. Multimeson production was further reduced by eliminating events in which any extra particles were detected in CLAS or the IC. The general method for choosing cut values was to vary them empirically over a coarse grid, taking into account the need to limit multimeson production and pick values that were close to minimizing the uncertainties in the final asymmetries.

1. Electron-pion missing mass cut

For both the $ep \to e\gamma\gamma p$ and $ep \to e\gamma\gamma(p)$ topologies, the electron-pion missing mass $M_x^{e\pi}$ should be equal to the proton mass of 0.938 GeV. In general, one would like the upper cut on $M_x^{e\pi}$ to be well below $M + m_\pi = 1.08$ GeV, to avoid contributions from multipion production. Placing tighter cuts helps to reduce the nuclear background.

The distribution in $M_x^{e\pi}$ is shown for the fully exclusive topology $ep \to e\gamma\gamma p$ in Fig. 2(b) averaged over the full kinematic range of the experiment. All other applicable exclusivity cuts have been applied. The solid circles correspond to counts from the ammonia target, while the open circles correspond to counts from the carbon target, scaled by the ratio of luminosities on $A > 2$ nucleons. A clear peak is seen near the nucleon mass from the ammonia target, with a smaller but wider distribution from the carbon target that matches the wings on the ammonia distributions on the low-mass side of the peak. On the high side of the peak, the ammonia rates are higher, due to the radiative tail of the single-pion production, and the gradual turn-on of multipion production. The vertical dashed lines show the cuts used: $0.84 < M_x^{e\pi} < 1.04$ GeV. Within the cut region, approximately 10% of the events come from nucleons in nuclei with $A > 2$ and 90% from free protons.

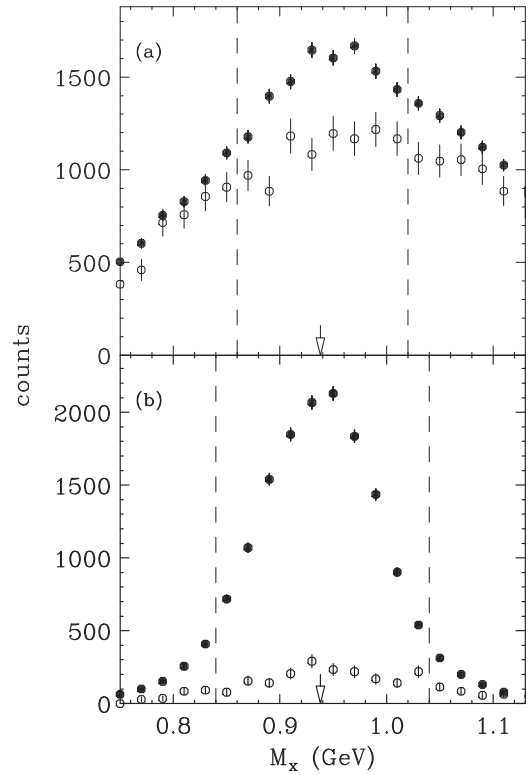

FIG. 2. Electron-pion missing mass spectra for the topologies (a) $ep \to e\gamma\gamma(p)$ and (b) $ep \to e\gamma\gamma p$. Counts from the ammonia target are shown as the solid circles and counts from the carbon target (scaled by the ratio of integrated luminosities on bound nucleons) are shown as the open circles. All other applicable exclusivity cuts have been applied. The vertical dashed lines indicate the cuts used.

The distribution in $M_x^{e\pi}$ is shown for topology $ep \to e\gamma\gamma(p)$ in Fig. 2(a), for $W < 1.5$ GeV. The nuclear background is considerably larger in this case, because there are no other exclusivity cuts that can be applied for this topology. For this reason, we used tighter missing mass cuts of $0.86 < M_x^{e\pi} < 1.02$ GeV. For $W > 1.5$ GeV, an increasingly large multipion background was observed, and those events were not used in the analysis.

The spectra were examined to see if the optimal cut values depends on W, Q^2, $\cos(\theta^*)$, or ϕ^*. Although the peak widths vary somewhat with kinematic variables, a constant cut value did not degrade the signal-to-noise ratios by more than a few percent.

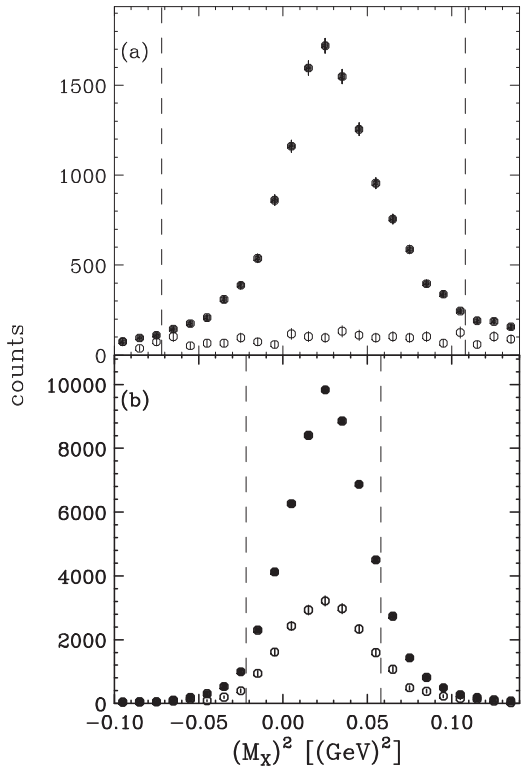

FIG. 3. Distribution of $(M_x^{eN})^2$ for (a) the topology $ep \to e\gamma\gamma p$ and (b) the topology $ep \to e\gamma(\gamma)p$. Symbols are as in Fig. 2. The vertical dashed lines show the cuts used. All other relevant exclusivity cuts have been applied.

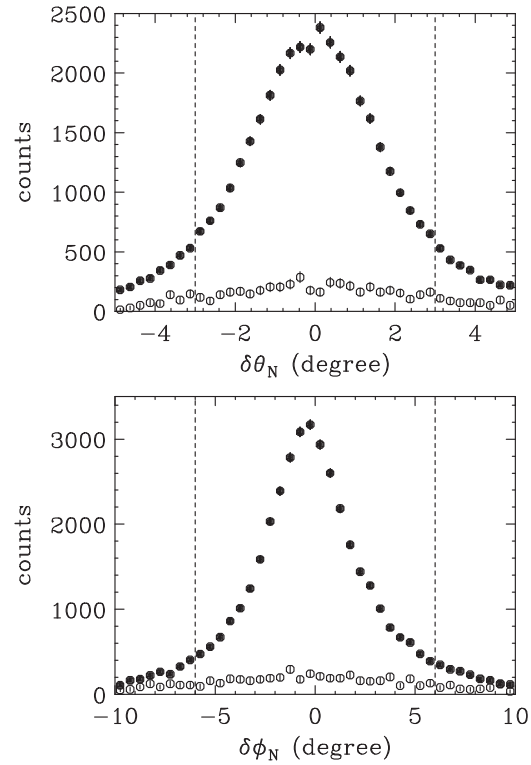

FIG. 4. Distribution of the in-plane (out-of-plane) angular difference in the predicted and observed proton direction cosines for the topology $ep \to e\gamma\gamma p$ are shown in the upper (lower) panel. The solid black points are for the ammonia target, while the open circles are from the carbon target, scaled by integrated luminosity. The vertical dashed lines indicate the cuts used in the analysis. All other relevant exclusivity cuts have been applied.

2. *Electron-proton missing mass cuts*

In the two topologies for which a proton was measured in the final state, the squared electron-proton missing mass $(M_x^{eN})^2$ should equal the π^0 mass squared (0.02 GeV^2). The spectra for the two topologies are shown in Fig. 3, averaged over the kinematic range of the experiment. The cuts were chosen symmetrically around 0.02 GeV^2, are shown as the vertical dashed lines, and correspond to $-0.07 < (M_x^{eN})^2 < 0.11$ GeV^2 for topology $ep \to e\gamma\gamma p$ and $-0.02 < (M_x^{eN})^2 < 0.06$ GeV^2 for topology $ep \to e\gamma(\gamma)p$. These cuts are very effective in reducing nuclear background, as well as eliminating multimeson production. The larger tails at positive values of $(M_x^{eN})^2$ are the result of photon radiation by the incoming or scattered electron.

3. *Proton angular cuts*

In the topology $ep \to e\gamma\gamma p$, cuts on the cone angles of the detected proton are useful in rejecting background from $A > 2$ materials. From the kinematics of the detected electron and pion, the direction cosines of the recoil proton are calculated and compared with the observed angles. We denote the difference in predicted and observed angles as $\delta\theta_N$ in the in-plane direction and $\delta\phi_N$ in the out-of-plane direction (which tends to have worse experimental resolution). Distributions of these two quantities are shown in Fig. 4. It can be seen that with cuts on M_x and the complementary angle, the nuclear background is relatively small and flat compared to the peaks from the free proton. We used the cuts $|\delta\theta_N| < 3^\circ$ and $|\delta\phi_N| < 6^\circ$, for all kinematic bins.

4. *Specific cuts used for topology $ep \to e\gamma(\gamma)p$*

Four cuts were applied for the $ep \to e\gamma(\gamma)p$ topology. The first was to require that the electron-proton-photon missing mass squared $(M_x^{ep\gamma})^2$ be close to zero, to ensure that the missing particle (if any), is a photon. The spectra at low and high W values are shown in Fig. 5, along with the cut $-0.02 < (M_x^{ep\gamma})^2 < 0.02$ GeV^2.

Two cuts for $ep \to e\gamma(\gamma)p$ were used to reduce contamination from events from the virtual Compton scattering (VCS) reaction $ep \to ep\gamma$. The VCS reaction differs from π^0 production by (a) electron-proton-photon missing energy $E_{\rm miss} = 0$ and (b) the difference in angle between the observed photon and the angle predicted from the detected electron and proton $\delta\theta_\gamma = 0$. For π^0 production, both of these quantities are positive. In addition, the photon energy on average is much larger for VCS than for π^0 production.

The features of VCS events can be readily seen in Fig. 6 as a strong enhancement at small values of both $\delta\theta_g$ and $E_{\rm miss}$, especially for events with photon energies greater than 2 GeV [Fig. 6(a)], with weaker population in this region for lower photon energies [Fig. 6(b)]. The dashed lines indicate the cuts

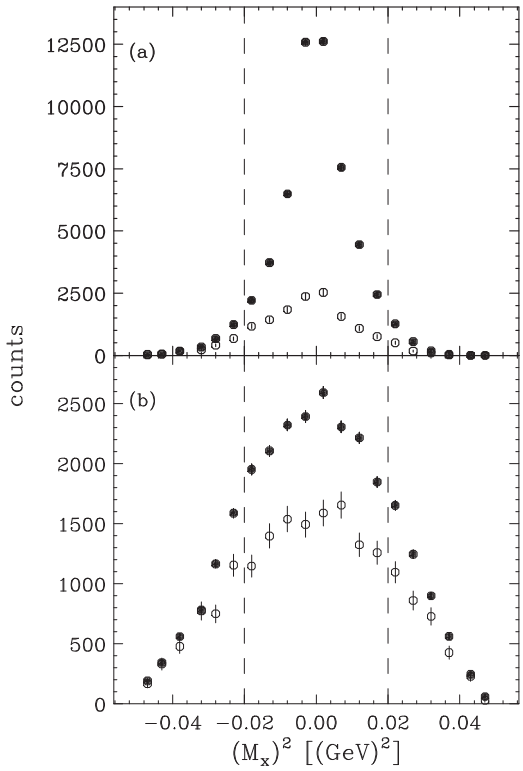

FIG. 5. Distributions of electron-proton-photon missing mass squared for the $ep \to e\gamma(\gamma)p$ topology for (a) $1.1 < W < 1.45$ GeV and (b) $2.15 < W < 2.5$ GeV. Symbols are as in Fig. 2. The vertical dashed lines show the cuts used. All other relevant exclusivity cuts have been applied.

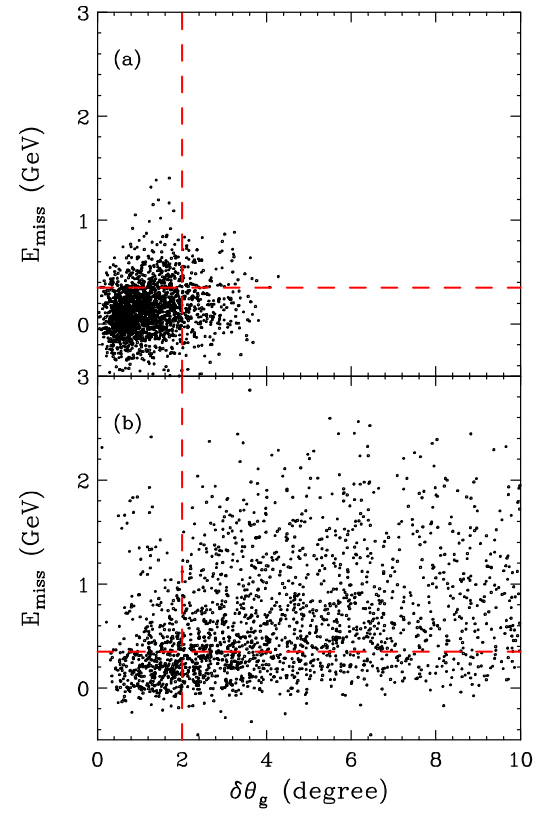

FIG. 6. Distributions of angular difference between the predicted and measured photon (horizontal axis) vs electron-proton-photon missing energy (vertical axis) for the $ep \to e\gamma(\gamma)p$ topology. Panel (a) is for photons with energy greater than 2 GeV, with the remainder of the events in panel (b). The dashed lines indicate the two cuts used in the analysis. All other exclusivity cuts have been applied.

used in the analysis. The cuts were applied differently for high and low photon energies:

$$\delta\theta_g > 2 \text{ deg AND } E_{\text{miss}} > 0.35 \text{ GeV for } E_\gamma > 2 \text{ GeV}, \tag{2}$$

$$\delta\theta_g > 2 \text{ deg OR } E_{\text{miss}} > 0.35 \text{ GeV for } E_\gamma < 2 \text{ GeV}. \tag{3}$$

With all other exclusivity cuts applied, the above cuts remove 97% of the events for $E_\gamma > 2$ GeV and 5% of the events for $E_\gamma < 2$ GeV.

Another cut was used to reject events where the actual reaction was not from electron scattering but rather a photoproduction reaction, i.e., $\gamma p \to pe^-\gamma(e^+)$, where the γ, e^-, and missing e^+ come from π^0 Dalitz decay. In this case, the opening angle between the electron and positron is zero. Such events result in an enhancement in the difference in azimuthal angles between the measured electron and the missing positron (calculated assuming the missing particle is a photon). We put a cut of ± 30 deg to eliminate these rarely occurring events.

The final cut was on the quantity $M_{\gamma(\gamma)}$, which is the invariant mass of the detected photon and the missing particle, with the imposed constraint that the mass of the missing particle is zero. As shown in Fig. 7, the $M_{\gamma(\gamma)}$ spectrum is consistent with pure neutral pion production when all other

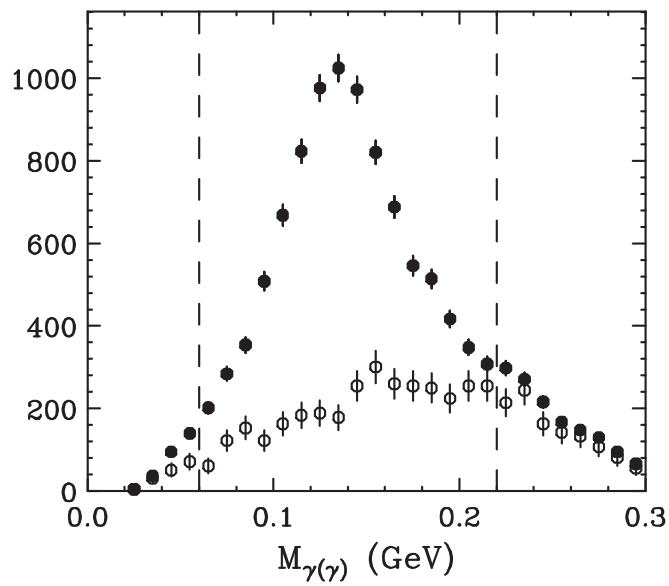

FIG. 7. Distribution of $M_{\gamma(\gamma)}$ for the topology $ep \to e\gamma(\gamma)p$. Symbols are as in Fig. 2. The vertical dashed lines show the cuts used. All other relevant exclusivity cuts have been applied.

exclusivity cuts are applied. We used the cut $0.06 < M_{\gamma(\gamma)} < 0.22$ GeV.

5. Additional cuts

For topology $ep \to e\gamma\gamma p$, the energy of all final-state particles is measured, and therefore the missing energy E_m distribution is centered on zero for free proton events and about 0.02 GeV for bound protons. A cut of $E_m < 0.13$ GeV was used to give a slight improvement in the signal-to-noise ratio. For topology $ep \to e\gamma\gamma(p)$, only events with $W < 1.5$ GeV were used, as mentioned above. For topology $ep \to e\gamma(\gamma)p$, only events with the photon in the EC were used.

C. Kinematic binning

The kinematic range of the experiment is $1.1 < W < 3$ GeV and $1 < Q^2 < 6$ GeV^2. As shown in Fig. 1 of Ref. [1], the range in Q^2 changes with W. We therefore made four bins in Q^2, where the limits correspond to electron scattering angles of 15.5, 18, 21, 26, and 38 deg. We used fixed W bins of width 0.05 GeV for $W < 1.9$ GeV, which is comparable to the experimental resolution. For $W > 1.9$ GeV, the bin widths gradually increase to achieve roughly equal counting rates, with bin boundaries at 1.90, 1.96, 2.03, 2.11, 2.20, 2.31, 2.43, 2.56, 2.70, 2.85, and 3 GeV. We used six bins in $\cos(\theta^*)$, with boundaries at -0.6, -0.2, 0.1, 0.36, 0.6, 0.85, and 0.995. We used 12 bins in ϕ^*, equally spaced between 0 and 2π.

A strong consideration in choosing the bin sizes was that we required at least ten counts in a given bin in order to have approximately Gaussian statistical uncertainties. The total number of bins is 7488, of which about 5700 had enough events to be included in the final results.

III. ASYMMETRIES

Spin asymmetries were formed as follows:

$$A_{LL} = \frac{N^{\uparrow\downarrow} + N^{\downarrow\uparrow} - N^{\uparrow\uparrow} - N^{\downarrow\downarrow}}{N_{\rm tot}\ f\ P_B P_T}, \tag{4}$$

$$A_{UL} = \frac{N^{\uparrow\uparrow} + N^{\downarrow\uparrow} - N^{\uparrow\downarrow} - N^{\downarrow\downarrow}}{N_{\rm tot}\ f\ P_T}, \tag{5}$$

where the symbols N represent the number of events in a given helicity configuration, divided by the corresponding integrated beam current. The first superscript $\uparrow$ refers to the beam polarization direction and the second to the target polarization direction. The total number of counts is denoted by $N_{\rm tot} = N^{\uparrow\uparrow} + N^{\downarrow\uparrow} + N^{\uparrow\downarrow} + N^{\downarrow\downarrow}$, and f is the dilution factor, defined as the fraction of events originating from polarized free protons, compared to the total number of events. The product of beam polarization (P_B) and target polarization (P_T) as well as the value of P_B are listed in Table I for the two parts of the experiment.

A. Dilution factor

The dilution factor f is defined as the ratio of spin-averaged scattering rate from free nucleons to the scattering rate from all nucleons in the target. With the assumption that the cross section per nucleon is the same for bound protons in all of the nuclear materials (with $A > 2$) in a given target, and also that the effective detection efficiency is the same for the ammonia and carbon targets, then

$$f = 1 - R_{A>2}\frac{N_C}{N_{NH_3}}, \tag{6}$$

where N_C and N_{NH_3} are the number of counts from the carbon and ammonia targets respectively, measured in a given kinematic bin for a given topology, normalized by the corresponding integrated beam charge. The symbol $R_{A>2}$ denotes the ratio of the number of bound nucleons in the ammonia target to the number of bound nucleons in the carbon target. Bound nucleons are defined to be in materials with atomic number $A > 2$. The latter was determined from a detailed analysis of the target composition using inclusive electron-scattering rates from ammonia, carbon, and empty targets, yielding $R_{A>2} = 0.71$ for part A and $R_{A>2} = 0.72$ for part B.

Because the integrated luminosity on the carbon target was about ten times lower than on the ammonia target, there is a large amplification of the uncertainty on the ratio of carbon to ammonia counts, $\frac{N_C}{N_{NH_3}}$. In many cases, this would lead to unphysical values of f (i.e., $f < 0$). We therefore took advantage of the fact that f is a very slowly varying function of kinematic variables and did a global fit to $\frac{N_C}{N_{NH_3}}$. The fit values were then used to evaluate f in each kinematic bin.

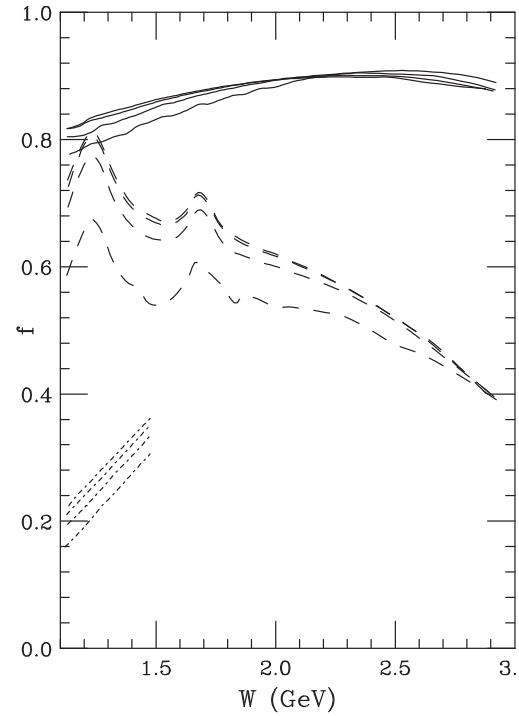

FIG. 8. Dilution factors as a function of W for the $ep \to e\gamma\gamma p$ topology (solid curves), the $ep \to e\gamma(\gamma)p$ topology (long dashed curves), and the $ep \to e\gamma\gamma(p)$ topology (short dashed curves) for the four Q^2 bins of this experiment and a typical bin in $\cos(\theta^*)$. For the two sets of dashed curves, smaller values of f correspond to higher values of Q^2.

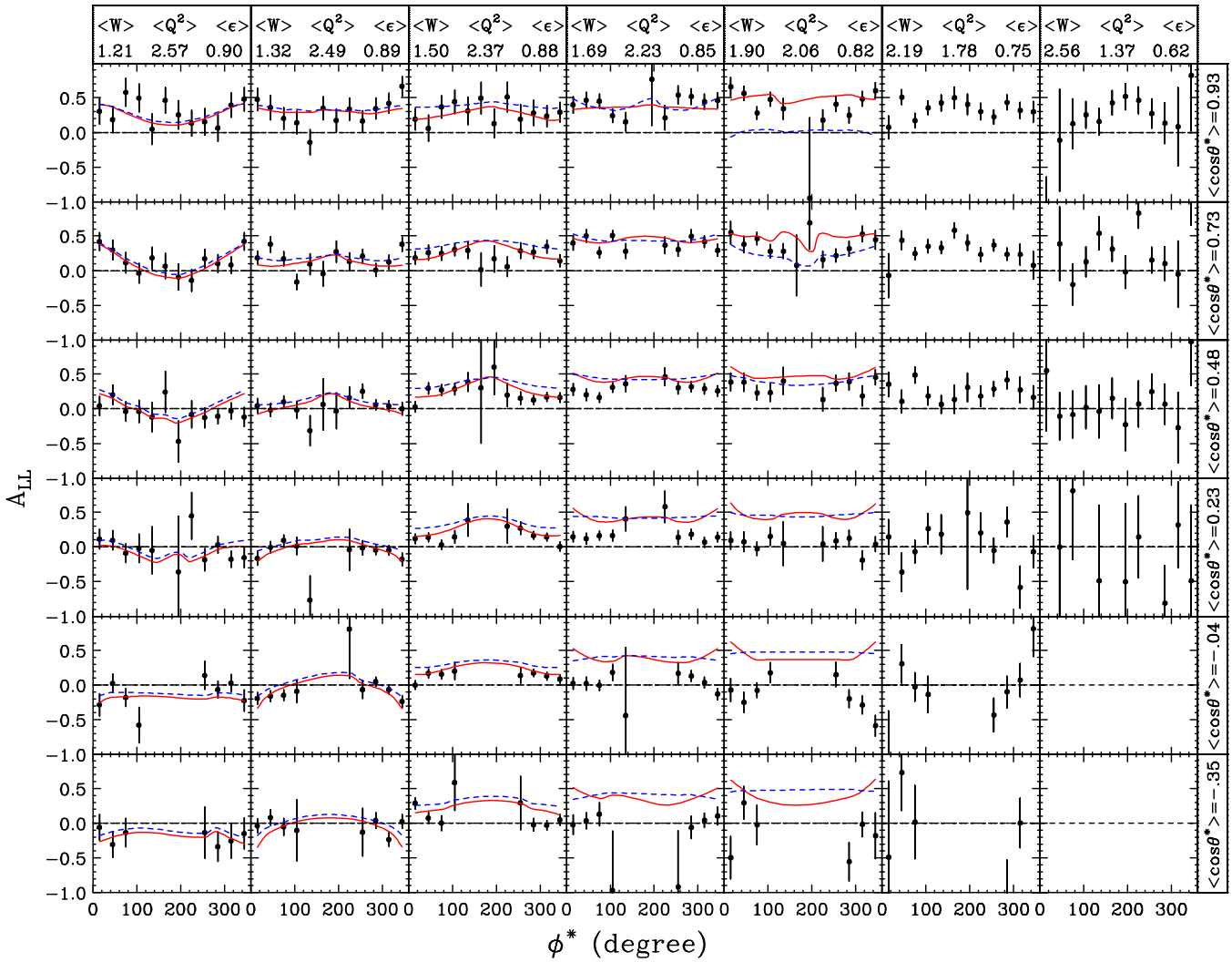

FIG. 9. Beam-target double spin asymmetry A_{LL} for the reaction $ep \to e\pi^0 p$ as a function of ϕ^* in seven bins in W (columns) and six $\cos(\theta^*)$ bins (rows). The results are from the two lower Q^2 bins of this analysis. The column headings include the average value of virtual photon polarization ϵ. The error bars reflect statistical uncertainties only. The solid red curves are from the MAID 2007 fit [13] and the blue dashed curves are from a JANR fit [14].

As in Ref. [1], the functional forms for the fit contained 25 terms of the form $p_i \cos^{N_C}(\theta^*) W^{N_W}(Q^2)^{N_Q}$, where p_i is a free parameter, and the exponents N_C, N_W, and N_Q range from 0 to 3 (although not all possible terms were included). An additional eight terms were included to account for the influence of the three prominent nucleon resonances centered at 1.23, 1.53, and 1.69 GeV, all with widths of 0.120 GeV. The reason that these resonance terms are needed is that the nucleon resonances are effectively broadened in the target materials with $A > 2$ by Fermi motion. This generates resonant-like structures in the ratio of carbon-to-ammonia count rates. Tests were made to see if any ϕ^*-dependent terms would improve the fits. No significant improvements were found.

The dilution factors for part B for the three topologies are shown in Fig. 8 as a function of W for the four Q^2 bins of this analysis and a typical bin in $\cos(\theta^*)$. For the fully exclusive topology, $ep \to e\gamma\gamma p$, the dilution factor is large, about 0.85 on average, corresponding to the good rejection of background that is possible with the exclusivity cuts when the recoil proton is detected. For the topology $ep \to e\gamma(\gamma)p$, the dilution factor is reasonably good for $W < 2$ GeV, averaging about 0.65, with significant resonant structure visible. For $W > 2$ GeV, there is a trend for f to decrease, dropping to values as low as 0.4 at the highest values of W. This is because Fermi broadening results in an increasing amount of multipion production from the nuclear target material. The dilution factor for topology $ep \to e\gamma\gamma(p)$ is much lower than for the other two topologies, averaging about 0.25. The Q^2 dependence is relatively weak, although there is a trend towards lower values of f at higher values of Q^2. Because part A had much lower statistical accuracy than part B, we used the part B fits for part A.

B. Combining data sets

The entire asymmetry analysis was performed separately for parts A and B. The results were combined by averaging

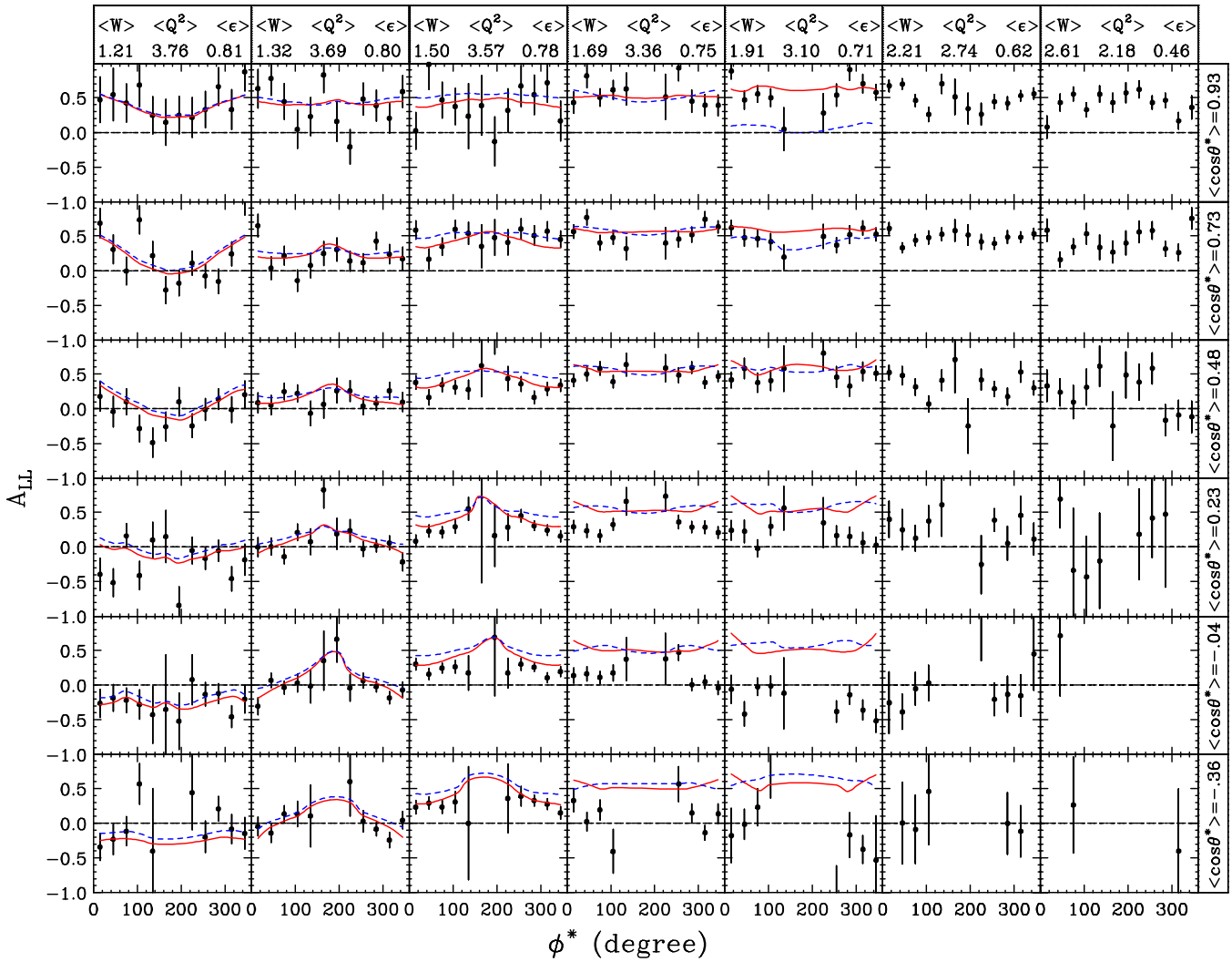

FIG. 10. Same as Fig. 9, except for the two larger Q^2 bins of this analysis.

asymmetries, weighted by their respective statistical uncertainties, for each of the 4-dimensional bins. Since the two configurations differ only in the acceptance function, which should cancel in forming the asymmetries, the expectation is that the acceptance functions should be fully compatible statistically. This expectation was verified for both asymmetries for all three topologies.

C. Combining topologies

We next averaged together the asymmetry results for the three topologies, weighted by their respective statistical uncertainties, for each of the 4-dimensional bins. For both asymmetries, the topologies were found to be statistically compatible, indicating that the dilution factors for the different topologies are properly accounted for. We found that topology $ep \to e\gamma\gamma p$ is the biggest contributor at high W, while topology $ep \to e\gamma(\gamma)p$ dominates at low values of W. Due to the poor dilution factor, topology $ep \to e\gamma\gamma(p)$ has relatively little impact on the final results.

D. Additional corrections

As summarized in Ref. [1], radiative corrections were found to be negligible. The correction from the slightly polarized nitrogen in the ammonia targets was also found to be negligible.

E. Systematic uncertainties

The dominant systematic uncertainty on all the asymmetry results is an overall scale uncertainty from the beam and target polarizations. The uncertainty in A_{LL} is relatively small (1.4%) because $P_B P_T$ was well measured using ep elastic scattering. The relative uncertainty in A_{UL} is larger (4%) due to the uncertainty in P_B, from which we obtained P_T by dividing $P_B P_T$ by P_B.

The other source of normalization uncertainty is the dilution factor. As discussed in more detail in Ref. [3], the uncertainties in the target composition correspond to about a 2.5% relative uncertainty in the amount of background subtraction, which corresponds to 1% to 1.5% in the asymmetry results, for the

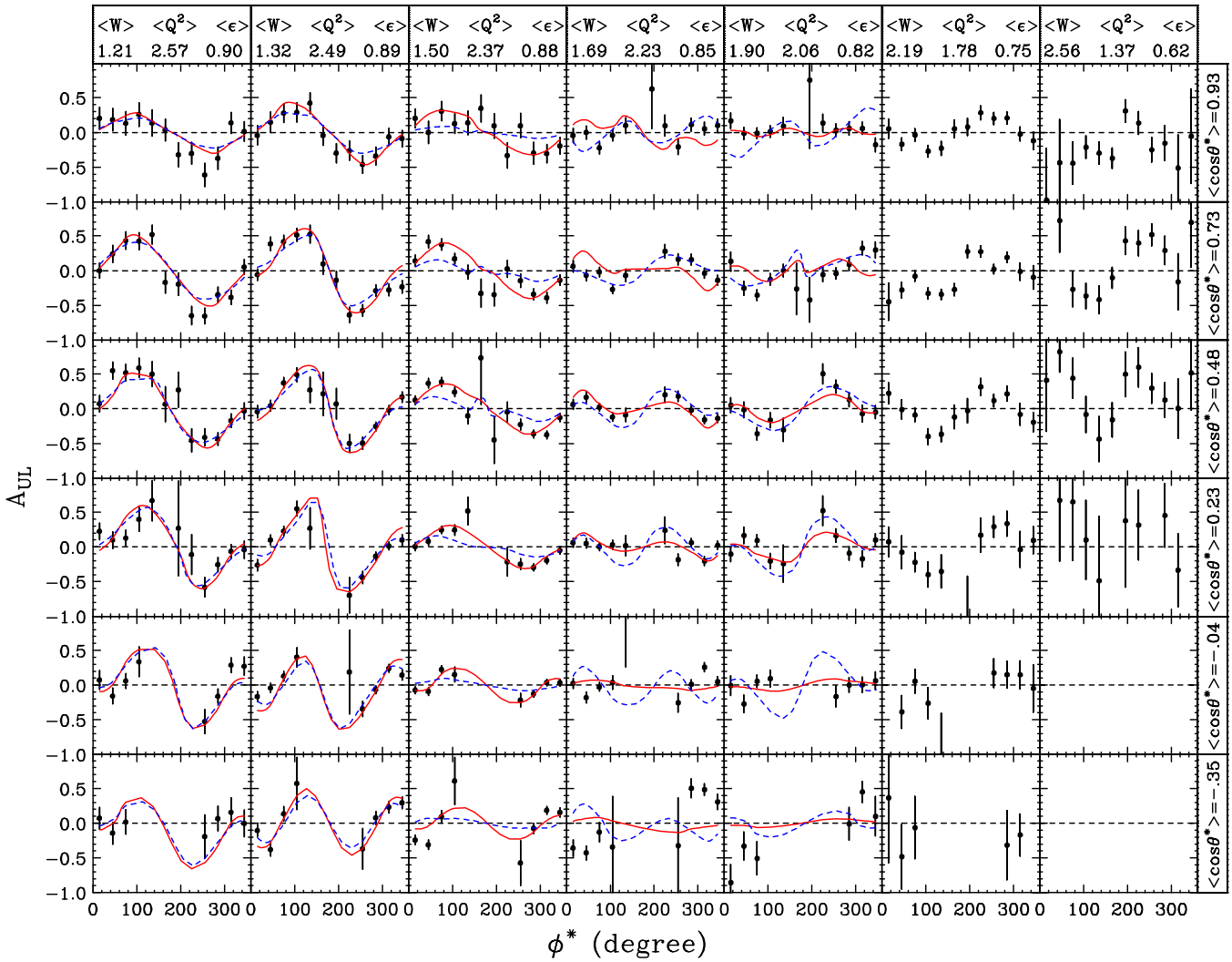

FIG. 11. Target single-spin asymmetry A_{UL} for the reaction $ep \to e\pi^0 p$ as a function of ϕ^* in seven bins in W (columns) and six $\cos(\theta^*)$ bins (rows). The results are from the two lower Q^2 bins of this analysis. The error bars reflect statistical uncertainties only. The solid red curves are from the MAID 2007 fit [13] and the blue dashed curves are from a JANR fit [14].

missing particle topologies, and less than 0.5% for the fully exclusive topology.

Another source of systematic uncertainty is in the factor $R_{A>2}$. We compared three methods of determining this factor: a study of inclusive electron scattering rates, fits to the low electron-pion missing mass spectra, and the value that gives the best agreement for A_{LL} between the fully exclusive topology and the topology where the recoil nucleon is not detected. This last technique relies on the fact that the fully exclusive topology has much less nuclear background. From these comparisons, we estimate a systematic uncertainty of about 2% (relative) for $R_{A>2}$. This translates into approximately 1.5% (at low W) to 2.5% (at high W) overall normalization uncertainties on both A_{LL} and A_{UL}.

It is also possible for assumptions made in the dilution factor fitting, such as the lack of ϕ^* dependence, to result in point-to-point systematic uncertainties. Based on trying out several different functional forms to the fit, these were found to be much smaller than the point-to-point statistical uncertainties. Adding the above sources of uncertainty in quadrature, we obtain an overall normalization uncertainty of 3% for A_{LL} and 5% for A_{UL}.

IV. RESULTS

With over 5700 kinematic points, each with relatively large statistical uncertainties, it is a challenge to portray the entire data set in a meaningful way. For plotting purposes, we therefore averaged together adjacent bin triplets or quartets in W and adjacent bin pairs in Q^2. The complete set of results is available in the CLAS database [11] and in the Supplemental Material associated with this article [12].

A. A_{LL}

The results for the beam-target spin asymmetry A_{LL} are plotted as a function of ϕ^* in seven bins in W and six bins in $\cos(\theta^*)$ in Fig. 9 for the lower Q^2 data and in Fig. 10 for the

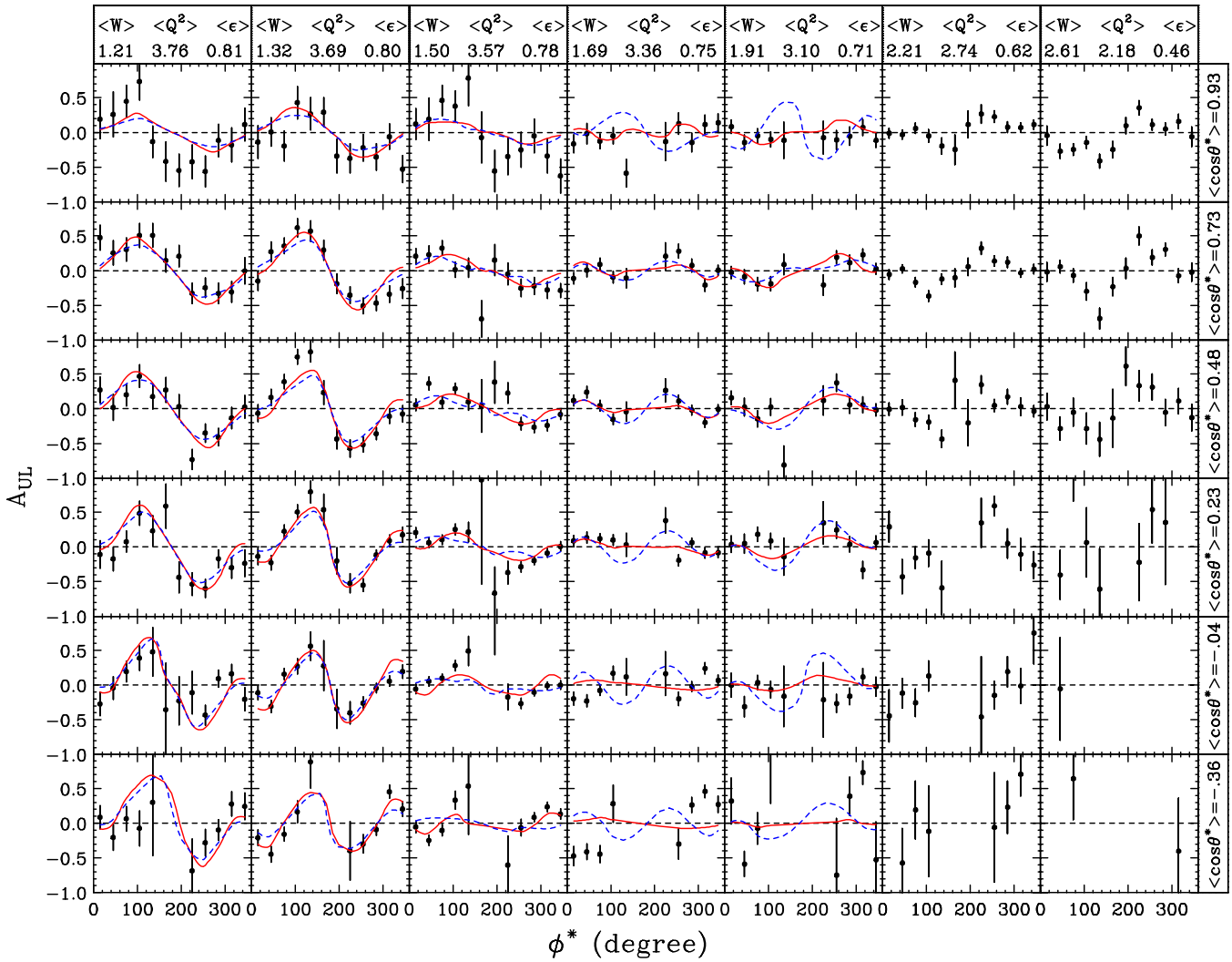

FIG. 12. Same as Fig. 11, except for the two larger Q^2 bins of this analysis.

higher Q^2 data. A weak trend for larger asymmetries at larger Q^2 can be observed.

The main features of the data are a relatively large and positive asymmetry (averaging about 0.3) for most kinematic bins. A major exception is for the lowest W bin, centered on the $\Delta(1232)$ resonance, where the values of A_{LL} are closer to zero. This feature is expected because the $\Delta(1232)$ transition is dominated by spin-1/2 to spin-3/2 transitions, which gives a negative value of A_{LL}, balancing the positive contribution from the Born terms. Another exception is for the lowest $\cos(\theta^*)$ bins, where again the asymmetries are close to zero.

Also shown on the plots are the results of two representative fits to previous data (limited to $W < 2$ GeV): the 2007 version of the MAID unitary isobar fit [13] and the unitary isobar version of the joint analysis of nucleon resonances (JANR) fit [14], averaged with the same weighting as the data points. Formally, these two fits are rather similar in nature, but differ in the data sets used and in the functional forms used for the Q^2 dependence of the resonance form factors. By and large, both the MAID 2007 and the JANR fits describe the data reasonably well up to $W = 1.6$ GeV, with differences appearing at larger W. Compared to the asymmetries for exclusive π^+ electroproduction from this same experiment (see figures in Ref. [1]), the π^0 asymmetries are generally closer to zero, except at forward angles and larger values of W, where they are very similar.

B. A_{UL}

The results for the target spin asymmetry A_{UL} are plotted as a function of ϕ^* in seven bins in W and six bins in $\cos(\theta^*)$ in Fig. 11 for the lower Q^2 data and in Fig. 12 for the higher Q^2 data. It can be seen that the Q^2 dependence of the results is weak. The main feature of the data is large $\sin(\phi^*)$ modulations that are small at forward angles and grow to nearly maximal values at central angles. At low values of W, the modulations are almost equal in magnitude, but of opposite sign, to those observed for π^+ electroproduction (see corresponding figures in Ref. [1]), while at large values of W, the sign of the modulations changes from the low W asymmetries to be in agreement with the π^+ asymmetries.

The sign and magnitude of the results are well reproduced by the MAID and JANR fits for $W < 1.6$ GeV. At larger W, the MAID fit reproduces the relatively small asymmetries observed in the data for $1.6 < W < 2$ GeV, while the JANR fit exhibits larger asymmetries than observed in the experiment. Combined with the results for A_{LL}, the results for A_{UL} strongly suggest that there are important nucleon resonance contributions to exclusive pion electroproduction for $W > 1.7$ GeV and $Q^2 > 1$ GeV^2.

V. SUMMARY

Target and beam-target spin asymmetries in exclusive π^0 electroproduction ($\gamma^* p \to p\pi^0$) were obtained from scattering of 6-GeV longitudinally polarized electrons from longitudinally polarized protons using the CLAS detector at JLab. The kinematic range covered is $1.1 < W < 3$ GeV and $1 < Q^2 < 6$ GeV^2. Results were obtained for about 5700 bins in W, Q^2, $\cos(\theta^*)$, and ϕ^*. Except at forward angles, very large target-spin asymmetries are observed over the entire W region. In contrast to π^+ electroproduction, the sign of the A_{UL} modulations changes from positive at low W to negative at high W. Reasonable agreement is found with the phenomenological MAID 2007 fit [13] and the JANR fit [14] to previous data for $W < 1.6$ GeV, but significant differences are seen at higher values of W, where no data were available when the fits were made. We anticipate that new global fits using the present π^0 target and beam-target asymmetry data, when combined with beam-spin asymmetry and spin-averaged cross-sectional data, as well as π^+ observables, will yield major insights into the structure of the proton and its many excited states.

ACKNOWLEDGMENTS

We thank I. Aznauryan for providing the JANR source code and L. Tiator for providing the MAID 2007 source code. We thank X. Zheng for suggesting the functional form of the dilution factor fit. We acknowledge the outstanding efforts of the staff of the Accelerator and the Physics Divisions at Jefferson Lab that made this experiment possible. This work was supported by the U.S. Department of Energy (DOE), the National Science Foundation, the Scottish Universities Physics Alliance (SUPA), the United Kingdom's Science and Technology Facilities Council, the National Research Foundation of Korea, the Italian Instituto Nazionale di Fisica Nucleare, the French Centre National de la Recherche Scientifique, and the French Commissariat à l'Energie Atomique. This material is based upon work supported by the U.S. Department of Energy, Office of Science, Office of Nuclear Physics, under Contract No. DE-AC05-06OR23177.

[1] P. E. Bosted *et al.* (CLAS Collaboration), Phys. Rev. C **94**, 055201 (2016).
[2] B. A. Mecking *et al.*, Nucl. Instr. Meth. **503**, 513 (2003).
[3] Y. Prok *et al.* (CLAS Collaboration), Phys. Rev. C **90**, 025212 (2014).
[4] E. Seder *et al.* (CLAS Collaboration), Phys. Rev. Lett. **114**, 032001 (2015); S. Pisano *et al.* (CLAS Collaboration), Phys. Rev. D **91**, 052014 (2015).
[5] V. V. Frolov *et al.*, Phys. Rev. Lett. **82**, 45 (1999).
[6] A. N. Villano *et al.*, Phys. Rev. C **80**, 035203 (2009).
[7] M. Ungaro *et al.*, AIP Conf. Proc. **1432**, 187 (2012).
[8] R. De Masi *et al.* (CLAS Collaboration), Phys. Rev. C **77**, 042201 (2008).
[9] A. S. Biselli *et al.* (CLAS Collaboration), Phys. Rev. C **68**, 035202 (2003); **78**, 045204 (2008).
[10] A. Kim *et al.* (CLAS Collaboration), arXiv:1511.03338 [nucl-ex] [Phys. Lett. B (to be published)].
[11] [clasweb.jlab.org/physicsdb]
[12] See Supplemental Material at http://link.aps.org/supplemental/10.1103/PhysRevC.95.035207 for plain text tables of asymmetry results for this experiment.
[13] [www.portal.kph.uni-mainz.de/MAID/]; D. Drechsel, O. Hanstein, S. S. Kamalov, and L. Tiator, Nucl. Phys. A **645**, 145 (1999).
[14] I. G. Aznauryan, Phys. Rev. C **67**, 015209 (2003); I. G. Aznauryan *et al.* (CLAS Collaboration), *ibid.* **80**, 055203 (2009).